INTERNATIONAL JOURNAL FOR NUMERICAL METHODS IN FLUIDS
Int. J. Numer. Meth. Fluids 2011; **67**:1373–1392
Published online 7 October 2010 in Wiley Online Library (wileyonlinelibrary.com). DOI: 10.1002/fld.2422

Adaptive Lagrangian–Eulerian computation of propagation and rupture of a liquid plug in a tube

Ez A. Hassan[1], Eray Uzgoren[2,‡], Hideki Fujioka[3,§], James B. Grotberg[4,¶] and Wei Shyy[1,5,*,†,‖]

[1]*Aerospace Engineering, University of Michigan, Ann Arbor, MI, U.S.A.*
[2]*Middle East Technical University, Northern Cyprus Campus, Mersin, Turkey*
[3]*Tulane University New Orleans, LA, U.S.A.*
[4]*Biomedical Engineering, University of Michigan, Ann Arbor, MI, U.S.A.*
[5]*Department of Mechanical Engineering, The Hong Kong University of Science and Technology, Clear Water Bay, Kowloon, Hong Kong*

SUMMARY

Liquid plug propagation and rupture occurring in lung airways can have a detrimental effect on epithelial cells. In this study, a numerical simulation of a liquid plug in an infinite tube is conducted using an Eulerian–Lagrangian approach and the continuous interface method. A reconstruction scheme is developed to allow topological changes during plug rupture by altering the connectivity information about the interface mesh. Results prior to the rupture are in reasonable agreement with the study of Fujioka *et al.* in which a Lagrangian method is used. For unity non-dimensional pressure drop and a Laplace number of 1000, rupture time is shown to be delayed as the initial precursor film thickness increases and rupture is not expected for thicknesses larger than 0.10 of tube radius. During the plug rupture process, a sudden increase of mechanical stresses on the tube wall is recorded, which can cause tissue damage. The peak values of those stresses increase as the initial precursor film thickness is reduced. After rupture, the peaks in mechanical stresses decrease in magnitude as the plug vanishes and the flow approaches a fully developed behavior. Increasing initial pressure drop is shown to linearly increase maximum variations in wall pressure and shear stress. Decreasing the pressure drop and increasing the Laplace number appear to delay rupture because it takes longer for a fluid with large inertial forces to respond to the small pressure drop. Copyright © 2010 John Wiley & Sons, Ltd.

Received 2 March 2010; Revised 10 August 2010; Accepted 11 August 2010

KEY WORDS: ALE; immersed boundary method; multi-phase flows; incompressible flow; mesh adaptation; laminar flow

1. INTRODUCTION

Lung airways are coated with a thin liquid film which keeps the underlying epithelial cells moist, protects airway tissue against infection, and contributes to the removal of dust particles. Under certain conditions, the liquid film can become thicker (e.g. congestive heart failure, asthma, emphysema, cystic fibrosis), have modified surface tension (e.g. surfactant deficiency in neonatal and adult

*Correspondence to: Wei Shyy, Aerospace Engineering, University of Michigan, Ann Arbor, MI, U.S.A.
†E-mail: weishyy@umich.edu
‡Assistant Professor.
§LONI Institute Computational Scientist.
¶Director.
‖Clarence L. 'Kelly' Johnson Collegiate Professor and Provost at HKUST.

respiratory distress syndrome) or develop different material properties, such as non-Newtonian fluid behavior, that appears in normal and abnormal mucus (asthma, cystic fibrosis). When these changes occur, surface tension forces can cause the film to become unstable, and create a liquid plug which occludes the airway. This process is called airway closure where the liquid plug blocks airways and reduces gas exchange, and enhances airway collapsibility. Also, the mechanical stresses induced by the plug propagation can cause pulmonary epithelial cells to be damaged [1].

Numerical investigations of liquid plug dynamics in a channel require modeling of interfacial conditions arising from the surface tension forces in addition to a well-equipped interface tracking method for the interface location. As reviewed by multiple authors [2–7], there are a vast number of studies in the literature featuring interface tracking methods classified into three main categories:

- Lagrangian methods [8–10] that modify grid to match interface location.
- Eulerian methods [7, 11–13] that extract the interface location with the help of a scalar function on a stationary grid.
- Eulerian–Lagrangian methods [6, 14, 15] that utilize a separate set of grid representing the interface on a stationary grid. Grid that represents the front can move freely based on the solution obtained on the stationary grid.

Once the location is known, the interfacial conditions can be applied in two distinct ways to impose the discontinuous pressure and viscous stresses across the interface as a result of the surface tension forces. According to multiple authors [2, 7, 16], these methods can be observed in two separate groups:

- Continuous interface methods [6, 14, 17, 18] (CIM) that solve one set of equations for all phases via smearing out the flow properties around the interface.
- Sharp interface methods [11, 19–22] (SIM) that impose the conditions directly on the interface by considering different sets of equations for different phases.

For each approach, there is a compromise between the computational cost and accuracy in capturing the interfacial dynamics [23]. Many of the studies on liquid plug propagation in a channel utilize the Lagrangian interface tracking method focusing only on the liquid phase.

Bilek *et al.* [24] investigated lung epithelial cell damage in a model of airway reopening, consisting of a semi-infinite bubble propagating in a narrow fluid-filled channel lined with pulmonary epithelial cells. They showed that cell damage increased with decreasing reopening velocity, and that the presence of a pulmonary surfactant prevented this injury. Using a single-fluid Lagrangian model, they demonstrated that as the air finger propagates over the cells lining the channel, walls experience different types of mechanical stresses such as shear stress, pressure, shear stress gradient and pressure gradient. They concluded that the steep pressure gradient near the finger front was the most likely cause of the observed cellular damage. Kay *et al.* [25] showed that cell damage was directly correlated with the pressure gradient, not the duration of stress exposure (period for a pressure wave to pass over a cell). Repeated reopening and closure was shown to damage the cell layer, even under conditions that would not lead to extensive damage from a single reopening event.

Studies by Bilek *et al.* [24] and Kay *et al.* [25] focused on the cell injury caused by air-finger replacement in liquid-filled airways equivalent to the rear half of a long liquid plug. Huh *et al.* [1] investigated mechanical injury of primary human small airway epithelial cells (SAECs) caused by propagation and rupture of liquid plugs. The micro-fluidic channel was lined with SAECs and a thin liquid film. Exposure of the SAECs to physiological fluid mechanical stresses associated with surfactant-deficient airway reopening led to significant cellular damage whose severity was elevated with increasing frequency of plug propagation and rupture. Furthermore, plug rupture imposed a higher risk of cellular injury than plug propagation alone. Additional experimental and theoretical studies on plug propagation in flexible microchannels by Zheng *et al.* [26] indicate higher risk of injury for greater flexibility, which is a feature of airways in emphysema, for example.

Howell *et al.* [27] modeled the propagation of a liquid plug through a compliant channel in the limit of Stokes flow and small capillary number. They obtained expressions for the pressure

DOI: 10.1002/fld

drop across the plug and the trailing film thickness as functions of the elastic properties of the channel, the capillary number, and the precursor film thickness. Their study showed that rupture (or reopening) is more likely to occur in a compliant channel coated with pre-existing thicker film. They also showed that increasing the longitudinal wall tension decreases the likelihood of rupture and that there is a critical pressure drop above which rupture occurs. Waters and Grotberg [28] considered the effect of soluble surfactant on the plug propagation through a single tube, and found that the surfactant activity increases the trailing film thickness and the pressure drop across the plug needed to move it at a prescribed velocity.

Fujioka and Grotberg [29, 30] used a finite volume method for a single-fluid Lagrangian formulation and considered the effects of inertia and surfactant. If the channel is wider than the plug length, the trailing film thickness is less than that of a semi-infinite bubble at the same Reynolds number (Re). The front meniscus develops a capillary wave whose amplitude increases with Re causing large variations in wall shear stresses and pressures, which can lead to a detrimental effect on the cells lining the airways. When surfactant is present, it accumulates on the front meniscus interface as it is swept from the precursor film. The surfactant concentration is at maximum somewhere in the front meniscus, and a surface tension gradient opposes the flow out of the film region. In this region, the surface velocity almost vanishes, and this results in the precursor film thickness near the meniscus being larger than the leading film. Because of an increase in the minimum film thickness, there is a reduction in the peaks of wall pressure and shear stress. However, in the thicker film region, the drag forces are actually larger than the surfactant-free case. Therefore, the pressure drop across the plug increases as the result of the increasing surfactant concentration.

Suresh and Grotberg [31] and Zheng *et al.* [32] considered the effect of gravity on the steady or quasi-steady motion of a liquid plug in a two-dimensional liquid-lined channel oriented at an angle α with respect to gravity, and found that the pre-bifurcation asymmetry of the plug increased with the plug length (L_p), capillary number (Ca) Re, but decreased with the Bond number (Bo). Fujioka *et al.* [8] and Uzgoren *et al.* [14] investigated unsteady liquid plug propagation numerically. They considered the propagation of a liquid plug within a rigid axisymmetric tube coated by a thin liquid film with and without surfactant. The magnitudes of the wall pressure and wall shear stress are greatest in the front meniscus region, and they increase with a thinner precursor film. If the trailing film is thicker (thinner) than the precursor film, the plug volume decreases (increases) as it propagates. When the plug length (L_P) becomes short, the Marangoni stress increases the hydrodynamic viscous friction and causes L_P to plateau. During the period of L_P plateau, since the meniscus surface curvature near the wall becomes strong, the pressure gradients and shear stress within the transition regions increase. The stability of the motion of a liquid plug is investigated by Campana *et al.* [33].

Fujioka *et al.* [8] investigated the propagation of a liquid plug based on the Lagrangian method, which works well until its rupture. At rupture, the break-up of the plug creates difficulties for Lagrangian approaches during the regridding process. Furthermore, when the precursor film becomes sufficiently thin, the liquid plug shrinks and the air fingers become closer to each other ultimately leading to rupture. As reported in [1], this scenario may lead to excessive stresses that damage pulmonary epithelial cells. Erneux and Davis [34] studied the critical film thickness at which the rupture of thin films occur. They have found that the critical thickness is directly related to the molecular forces and surface tension.

In this study, we further extend a Eulerian–Lagrangian technique reported earlier [14] to handle topological changes during the plug rupture to investigate stresses at the airway walls. Specifically, in order to handle topological changes of fluid–fluid interfaces, we have developed a reconstruction scheme based on altering connectivity information detailed in the computational procedure section.

Comparison with the previous Lagrangian model, up to the rupture, and the flow field and associated stress characteristics during and after rupture will be discussed. The liquid film thickness considered is $O(0.1)$ in comparison to the tube radius. In other words, we focus on relatively thick liquid films in this study.

DOI: 10.1002/fld

2. METHODOLOGY

2.1. Model description

Figure 1 shows a schematic of the computational model. A liquid plug propagates in a straight circular tube of radius R^*. The problem is assumed to be axisymmetric so that only (r, z) components are considered. The tube domain of $0<r^*<R^*$ and $-6R^*<(z^*-z_P^*)<6R^*$, is considered, where z_P^* is the middle of both tips. It is noted that the dimensional quantities are denoted by $*$. After non-dimensionalization, $*$ is removed. The pressure difference between left and right air bubbles drives the liquid plug with a constant surface tension. The liquid plug length, L_P, non-dimensionalized by the tube radius, is the distance between air bubble tips. The liquid film thickness for the front air bubble is denoted as h_2 whereas the trailing film thickness is denoted as h_1. They are also non-dimensionalized by the tube radius. The no-slip boundary condition is applied at the tube wall. Constant uniform air pressures of P_1^* and P_2^* are prescribed in cross-sections at $z=-6R^*$ and $6R^*$, respectively, while zero velocity condition is applied for the liquid film in the same cross-sections at $=-6R^*$ and $6R^*$. The dimensionless form of the Navier–Stokes equations and the continuity equation is:

$$\lambda\rho\left\{\left[\frac{\partial\mathbf{u}}{\partial t}\right]_{(r,z)}+(\mathbf{u}\cdot\nabla)\mathbf{u}\right\}=-\nabla p+\nabla\cdot[\mu\nabla\mathbf{u}+\mu(\nabla\mathbf{u})^{\mathrm{T}}]+\mathbf{F}_s \tag{1}$$

$$\nabla\cdot\mathbf{u}=0 \tag{2}$$

where $\mathbf{u}=\mathbf{u}^*/(\sigma^*/\mu_l^*)$ is the dimensionless fluid velocity vector, μ_l^* is the liquid viscosity, σ^* is surface tension of the air–liquid interface; $p=p^*/(\sigma^*/R^*)$ is the dimensionless pressure, R^* is the tube radius; $t=t^*/(\mu_l^*R^*/\sigma^*)$ is the time; $z=z^*/R^*$ and $r=r^*/R^*$. ρ and μ are the dimensionless density and the viscosity scaled by liquid ρ_l and μ_l, respectively With the density and viscosity of the gas kept constant, $\rho=1.3e-3$ and $\mu=4e-4$ for the baseline case. A key dimensionless parameter $\lambda=\rho_l^*\sigma^*R^*/\mu_l^{*2}$ is the Laplace number ($\lambda^{-1/2}$ is often called the Ohnesorge number). It involves the fluid properties and the tube diameter, and serves to characterize the plug and the associated fluid dynamics. The body force term, $\mathbf{F}_s$, in the present context is used to represent the surface tension, and will be discussed further.

To compare with the previous study of Fujioka *et al.* [8], which focused on the plug dynamics prior to the rupture, the same initial condition is employed. At $t=0$, a stationary liquid plug of length L_{P0} begins to move due to a constant driving pressure force. Since the velocity is initially set to zero in the entire domain, the pressure in each air phase should be uniform so that the initial driving pressure is $\Delta P=P_1-P_2$. The initial plug shape is approximated by a hemi-sphere of radius $1-h_2$ for front and rear menisci, the length between both meniscus tips L_{P0}, and a uniform film thickness of h_2 on both sides of the plug.

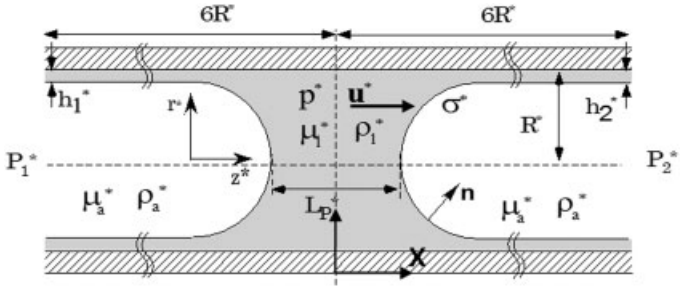

Figure 1. Computational setup and the boundary conditions, x axis attached to plug center before rupture and to the wall afterwards. Plug moves to the right.

DOI: 10.1002/fld

2.2. Computational procedure

The marker-based immersed boundary method employs Eulerian and Lagrangian variables to perform the interfacial flow computations. The Eulerian quantities are solved on a fixed background grid in the computational frame, whereas the Lagrangian quantities arise due to the marker points defined on the interface which can move freely. A single-fluid formulation for all fluid phases is made possible by smearing the properties across the interface.

Here the computational frame is set to follow the coordinate with the plug velocity $\mathbf{U}=(U,0)$, which is the average of both tip velocities. After rupture, the computational frame is fixed to the wall and the plug is allowed to move within it. From this point forward, discussion and results will be presented in terms of x instead of z because it is more convenient to represent an infinite tube. The x-coordinate in this frame, (x,r), is defined as follows:

$$x=\begin{Bmatrix} z-z_p & t\leqslant t_{\text{rupture}} \\ z-z_{p,\text{rupture}} & t>t_{\text{rupture}} \end{Bmatrix} \tag{3}$$

where z_p is the z position of the center of the plug and $z_{p,\text{rupture}}$ is z_p at the moment of rupture. t_{rupture} is the time at which rupture occurs. This definition guarantees that the plug is located at the center of the computational domain until t_{rupture} after which it is free to move.

The time derivative term in Equation (1) is redefined in terms of the computational node point (r,x)

$$\begin{aligned} \lambda\rho\left\{\left[\frac{\partial\mathbf{u}}{\partial t}\right]_{(r,x)}+[(\mathbf{u}-\mathbf{U})\cdot\nabla]\mathbf{u}\right\} &= -\nabla p+\nabla\cdot[\mu\nabla\mathbf{u}+\mu(\nabla\mathbf{u})^{\mathrm{T}}]+\mathbf{F}_S, \quad t\leqslant t_{\text{rupture}} \\ \lambda\rho\left\{\left[\frac{\partial\mathbf{u}}{\partial t}\right]_{(r,x)}+(\mathbf{u}\cdot\nabla)\mathbf{u}\right\} &= -\nabla p+\nabla\cdot[\mu\nabla\mathbf{u}+\mu(\nabla\mathbf{u})^{\mathrm{T}}]+\mathbf{F}_S, \quad t>t_{\text{rupture}} \end{aligned} \tag{4}$$

The source term in Equation (4), $\mathbf{F}_S$, represents the condition at the interfaces due to the surface tension.

2.3. Surface tension treatment

The surface tension effect in volumetric form, $\mathbf{F}_S$ in Equation (4), involves curvature (κ), surface normal ($\mathbf{n}$), and the Dirac delta function, $\delta\left(\frac{\mathbf{x}-\mathbf{X}}{\Delta x}\right)$, as given in Equation (5)

$$\mathbf{F}_S=\int_S Ca^{-1}\kappa\mathbf{n}\delta\left(\frac{\mathbf{x}-\mathbf{X}}{\Delta x}\right)\mathrm{d}S \tag{5}$$

For curvature and other computations related to geometry, marker points placed on the interface are utilized. These marker points, represented in the Lagrangian framework with $\mathbf{X}$, are free to move in response to the flow field computed on the background grid, which is represented in the Eulerian framework with $\mathbf{x}$. The magnitude of the position vectors $\mathbf{x}$ and $\mathbf{X}$ is normalized by the cell size, Δx. The marker locations for the surface grid are computed using a simple advection scheme via Equation (6), where the marker velocities are interpolated from the Eulerian grid.

$$\frac{\partial\mathbf{X}}{\partial t}=\mathbf{u}(\mathbf{X}) \tag{6}$$

DOI: 10.1002/fld

The interpolation of the velocity field is performed with the help of a discrete form of the Dirac delta function, $\delta((\mathbf{x}-\mathbf{X})/\Delta x)$ given in Equation (7)

$$\delta\left(\mathbf{r}=\frac{\mathbf{x}-\mathbf{X}}{\Delta x}\right)=\left\{\begin{array}{ll}\frac{1}{8}\left(5-2|\mathbf{r}|-\sqrt{-7+12-4|\mathbf{r}|^2}\right), & 1\leqslant|\mathbf{r}|\leqslant 2\\ \frac{1}{8}\left(3-2|\mathbf{r}|+\sqrt{1+4|\mathbf{r}|-4|\mathbf{r}|^2}\right), & 0\leqslant|\mathbf{r}|\leqslant 1\\ 0, & |\mathbf{r}|>1\end{array}\right\} \tag{7}$$

This approximation, which is also utilized in calculating the surface tension term in Equation (5), ensures that mass and momentum are conserved for any conversion between the background grid (Eulerian) and markers points (Lagrangian) as shown by Peskin *et al.* [17] and Shyy *et al.* [2].

As the markers advance to new positions with time, they can be unevenly distributed on the interface leading to larger computational errors. To maintain the desirable numerical accuracy, the markers are rearranged by addition/deletion based on the background grid with no more than two markers in each computational cell. The details are described in [35].

2.4. Interface reconstruction scheme

Reconstruction of the interface due to rupture is triggered numerically when the plug length decreases to a critical value, $L_{p,\text{critical}}$, that is in the order of the smallest grid size. In reality, the critical length is several orders of magnitude smaller and is related to the molecular forces. Furthermore, as is well known, the rupture dynamics (the detailed break-up process) cannot be faithfully simulated entirely in the context of the continuum formulation. Since we do not consider any molecular aspects of the model, our treatment is, necessarily, phenomenological in nature. The current study focuses on the fluid physics immediately before and after the rupture. The computational results reported below do have adequate resolutions in the pre- and post-rupture instants.

The reconstruction scheme involves altering of the interface data, primarily marker connectivity, to accommodate the rupture. The minimum distance between the marker points on left and right bubbles is tracked. When this distance reduces to a value less than the critical length, $L_{p,\text{critical}}$, corresponding markers are removed.

To compute the distance between two bodies, a list-based algorithm identifies the markers to be used and a length-based coordinate mapping procedure is utilized to exclude markers not participating in topology change. In 2D, the coordinates are translated into 1D form by computing the length of the interface along its path. In Figure 2, the markers tagged with 1 and 2 can be excluded during the binary search for marker point tagged with 3 because the coordinate mapping identifies those as neighboring markers. On the other hand, the marker 4 is included in the search as the mapping will not qualify it as a neighbor of marker 3. Once the distance between markers 3 and 4 becomes less than the critical distance, two markers are removed to

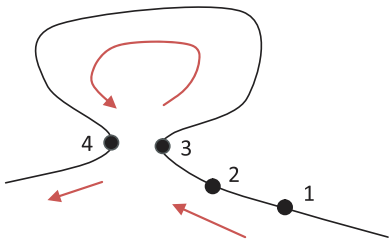

Figure 2. Identification of necking, a possible cause for topological change.

DOI: 10.1002/fld

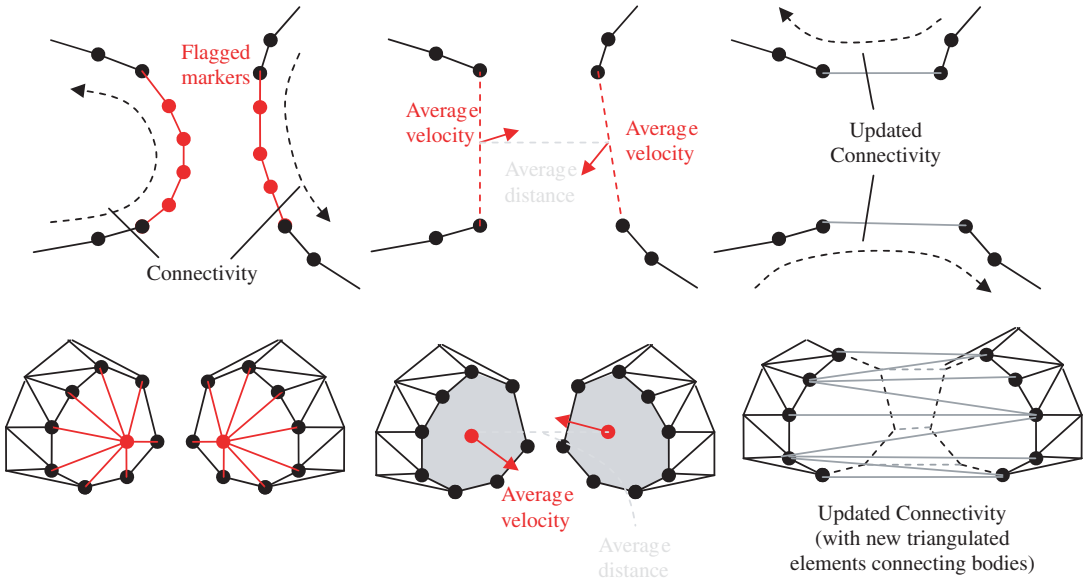

Figure 3. Summary of the reconstruction algorithm in 2D and 3D.

allow topological change. Overall, the triggers for the reconstruction algorithm are as follows: (Figure 3)

- Distance between markers in physical space should be smaller than the critical length.
- Distance between markers in surface coordinates should be larger than four computational cell lengths guaranteeing that the neighboring markers are excluded.
- Distance between the corresponding markers should decrease in time.

The third criterion utilizes marker velocities and is embedded into the reconstruction algorithm as a final check. The reconstruction scheme developed, involves the following steps:

- Markers flagged are removed. When the removed markers create a block (of markers), they are still represented by a single temporary element during this stage.
- Calculate the center and the average velocity of temporary elements.
- Check the distance between all other temporary elements.
- If the distance is less than the critical length, the connectivity information between the corresponding elements will be updated.

The connectivity update involves the following steps:

- A marker on the first temporary element is selected. Another marker on the other temporary element is selected based on its proximity to the initially selected marker.
- The nodes of the first element are ordered in counter clockwise direction, while the nodes of the second element are ordered in the clockwise direction.
- Following the ordered list of markers on temporary elements, create edges between the corresponding markers. The normal direction of the newly created elements is chosen in a way that they follow the normal direction of all the neighboring elements.

The markers which lose the connectivity information due to marker removal procedure in Figure 4 are connected to each other to accommodate topological change.

It should be noted that because the closest nodes are chosen for reconstruction in the finest region of the grid that mass conservation errors are kept to a minimum. In addition, the newly formed segments are reconstructed in a conservative manner such that there is always the same amount of fluid in each phase before and after marker addition/deletion. This procedure and validations are discussed in detail in [14, 15].

DOI: 10.1002/fld

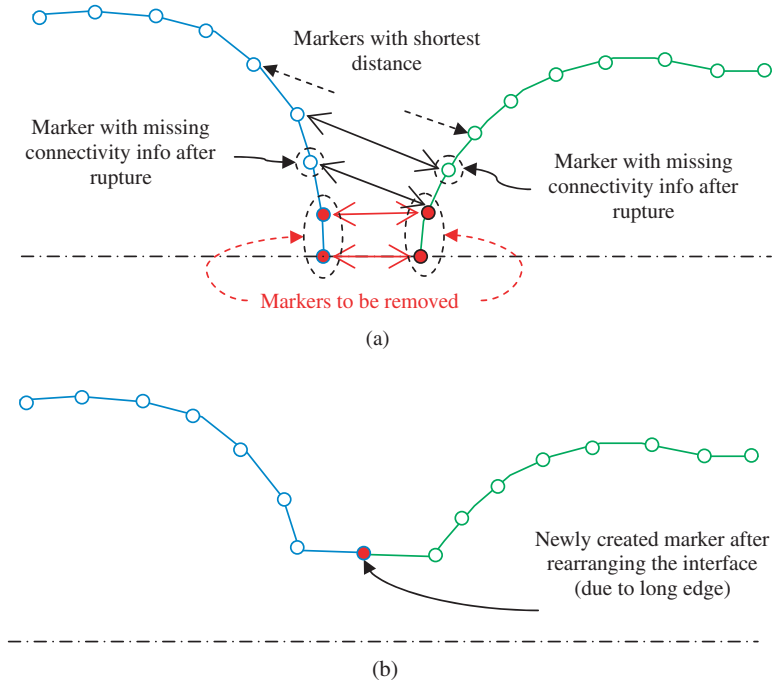

Figure 4. Reconstruction scheme: (a) Two interfaces come close so that the distance for the bottom markers are less than critical length and (b) forming a single interface by updating the connectivity information.

2.5. Local refinement of Eulerian grid

The described marker-based method solves a single set of equations for all the constituents, which brings rapid variations to flow variables and material properties around the interface. Resolving the whole domain to the desired length scale may result in unnecessary resolutions at regions far from the interface. In this study, an isotropically adaptive Cartesian grid is employed for solution of the flow governing equation. The grid is initialized in a uniform structure, which has prescribed number of cells in each coordinate direction. The cell that needs to be refined is split into four smaller and equal cells. This procedure brings additional levels of grids in which new coordinates in computational space are assigned to the level where cells reside. To ensure a smooth variation in grid cell-size for quality and simplicity, cells sharing a face are not allowed to differ by more than one level of refinement. The implementation details are described in [14].

All the cells cut by the interface are flagged for refinement. In addition to those cells, their neighboring cells (up to five layers) are also flagged for refinement to ensure the uniformity for proper smearing via the discrete Dirac delta function. This process of flagging and splitting cells is carried out recursively until the prescribed grid resolution around the interface is obtained. Figure 5 illustrates this refinement process.

In addition to interface-based grid adaptation, computational cells away from the interface are refined or coarsened based on the flow solution. The present implementation uses a phase-based vorticity criterion to determine critical cells for refinement or coarsening. A statistical mean and variation are computed for each phase. For the present study, the liquid phase is the main focus and consequently only cells containing liquid phase are considered for solution refinement. When the vorticity in a computational cell deviates from the mean by a value more than the specified variation, it is marked to be refined. On the other hand, computational cells with vorticity within 10% of the mean can be coarsened if four adjacent cells are found.

2.6. Adaptive time stepping

It should be noted that the numerical simulation of the rupture dynamics requires a numerical scheme that allows adaptive time stepping, especially to be able to capture the sudden changes in

DOI: 10.1002/fld

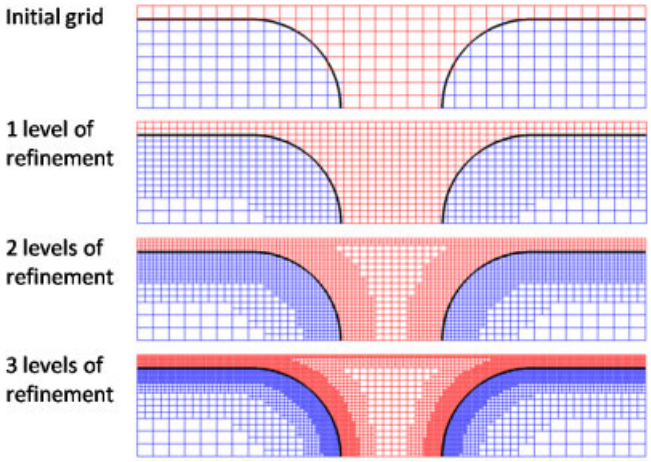

Figure 5. Geometry based grid refinement around the interface at various resolutions.

flow field in regard to shear stress and pressure. The present simulation adjusts the time step based on surface tension and the velocity field to restrict the marker movement to a single cell per time step. During the liquid rupture process, the time step can decrease by about a factor of 10.

3. RESULTS AND DISCUSSION

The two-fluid formulation presented above is utilized to investigate liquid rupture dynamics. The fluid physics associated with the velocity field, pressure and shear stress variations under various flow conditions, defined by the Laplace number (λ), initial plug length (L_{p0}) and initial precursor film thickness (h_2). The results will be compared with those of Fujioka *et al.* [36], which, uses the Lagrangian method and considers only the flow characteristics prior to the moment of rupture. The main components of the current computational framework have been previously utilized by Uzgoren *et al.* [14] and validated against steady plug propagation results in [29]. The present methodology can handle the topological change of the object, and the computation has been conducted to investigate the post-rupture dynamics. To ease the reading of the results, prior to rupture, the moving frame fixing to the center of the plug is used so that the results can be directly compared with those of Fujioka *et al.* [8]. After rupture, the stationary frame anchored by the wall is adopted, and the rupture plug is allowed to move within the reference frame.

3.1. Pre-rupture dynamics

First, the effect of initial precursor film thickness on plug length is studied to assess the current approach with that of the single-fluid formulation by Fujioka *et al.* [8]. The initial plug length and the non-dimensional pressure drop across the plug, ΔP, are taken as 1 at $\lambda = 1000$. Five cases are chosen based on the precursor film thickness, h_2, by setting it to 0.05, 0.07, 0.09, 0.10, and 0.13.

Figures 6(a) and (b) show the time-dependent variation of plug length at various initial precursor thicknesses, for $0 < t < 900$ and $0 < t < 60$ for magnified view, respectively. In the present study, the pressure drop is prescribed between the far left and right boundaries. At the initial stages of the simulation, the pressure drop is the primary force driving the liquid plug at an axial speed, $\boldsymbol{u}_z^*$ which, as shown in the non-dimensionalization procedure, can be represented by the local capillary number, $Ca = \boldsymbol{u}_z^*/(\boldsymbol{\sigma}^*/\boldsymbol{\mu}^*)$. The time history of the capillary number is presented in Figure 7(a) for $0 < t < 900$ and magnified view in Figure 7(b).

The interplay between the precursor thickness, h_2, and the trailing film thickness, h_1, influences the plug length as a result of the mass balance in the liquid phase. During the initial stage of the movement, the plug propagation speed, or Ca, increases at a near constant rate for all cases presented. The plug length also remains the same until $t = 8$, then the plug propagation speed starts

DOI: 10.1002/fld

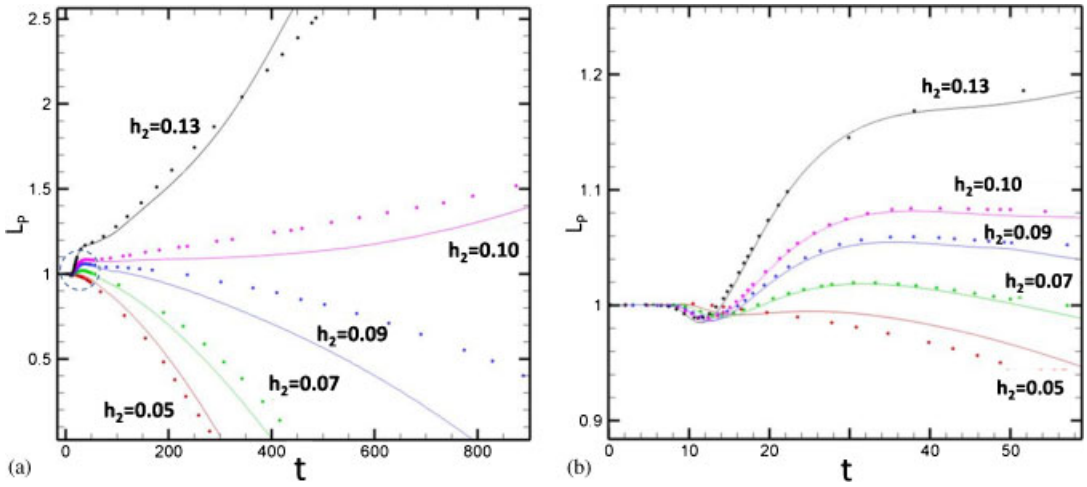

Figure 6. Plug length variation in time for various initial precursor film thickness values. Solid lines represent present study while dots represent study of [8]. (b) shows a more confined time domain to show details.

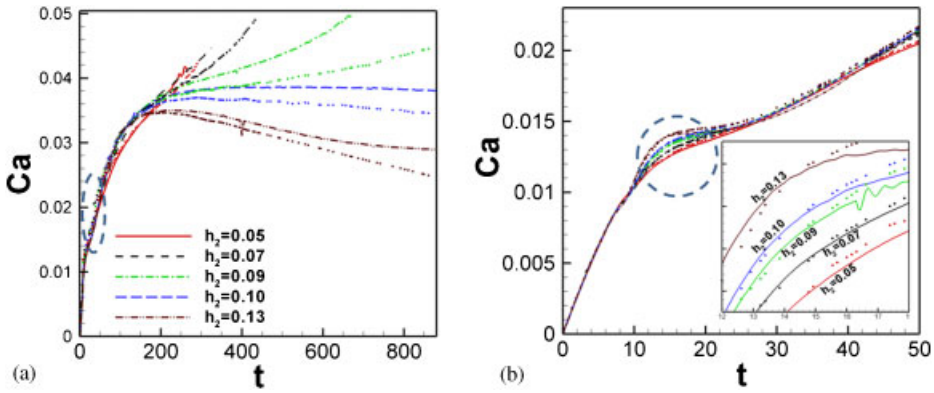

Figure 7. Course of plug speed, defined as the capillary number, in time for various initial precursor film thickness values. Solid lines represent present study while dots represent study of [8]. (b) shows progressively zoomed in views of the plot in (a).

to vary. In Figure 6(b), a similar variation is observed as the plug length decreases first, and then increases between $t=10$ and 20. The change in plug length can be interpreted as mass addition and removal, suggesting that as the plug widens, the precursor film thickness, h_2 becomes first larger than the trialing thickness, h_1 and then as the plug becomes narrower, h_2 becomes thinner that h_1. Figure 6(b) also shows that the variation in plug length appears earlier and faster for cases with larger initial precursor thicknesses. Consistent with the finding of Fujioka and Grotberg [29], the change in trailing film thickness is influenced mainly by the capillary number. As a result, when the plug length is at minimum in the early stages, *Ca* increases faster with larger precursor thicknesses. The overall trends seen in Figures 6(a) and 7(b) show that the liquid plug rupture is not expected with a precursor thickness 0.10 and higher. This behavior is reversed for $h_2=0.09$ and smaller provided that the rupture occurs at the same critical length. Accordingly, the rupture times are expected to be as follows: $t_R \approx 430$ for $h_2=0.07$; $t_R > 1000$ for $h_2=0.09$. As the initial precursor thickness becomes larger, the rupture is further delayed.

Figure 6 indicates that if $h_2<0.10$ rupture occurs. The above discussion is in agreement with single-fluid formulation of Fujioka *et al.* [8], which ignores the fluid motion associated with the gas phase. The difference between the two studies becomes more visible for $h_2=0.09$ and $h_2=0.10$, for which the dynamics of the liquid plug becomes very sensitive to the critical precursor thickness.

DOI: 10.1002/fld

In the single-fluid formulation the air pressure condition is directly applied at the liquid interface as constant pressure, whereas, in this study, it is applied at the far left and right domain boundary ($-6R*$ and $-6R*$, respectively). Although this value is small, the pressure variation within the gas phase is as high as 0.5% in ΔP at the meniscus tips of both gas bubbles. As the pressure drop at the bubble tips are different for the single- and two-fluid formulations by Fujioka *et al.* [36] and the present study, respectively, the two simulations are expected to show some differences. The differences between the two studies become more visible with larger initial h_2 values (hence stronger multi-phase effects near the wall), and as time progress (due to the unsteady accumulation of the pressure difference between the two studies). In Figure 7(a), the capillary number (the fluid velocity) continues to increase with $h_2 \leqslant 0.09$, whereas it shows a decrease with $h_2 \geqslant 0.10$ after $t > 100$. The decrease with $h_2 = 0.10$ is very slow, and approaches the steady-state case presented in [29] with a steady Ca number at 0.0385 and a steady L_p of 1.15. This is in contrast with the report of Fujiokat *et al.* [36], where the unsteady solution did not approach the steady case of [29]. This was accounted to the difference in L_p between the steady-state case of [29] and the unsteady one of [36] (presented with dots in Figure 6). Fujioka *et al.* [8] reported that as the plug length becomes larger than the steady plug length of 1.15, a constant Ca cannot be maintained. While qualitatively similar trends can be observed in Figures 6 and 7 between the present simulations and those of Fujiokat *et al.* [36], the mass transfer between the plug and the film and the dynamics in the gas phase result in observable differences and may suggest a larger L_p limit. Figures 6 and 7, one sees that for $h_2 = 0.09$ or lower, the plug moves faster while reducing L_p (for $t > 40$) indicating that the plug is losing mass. These figures suggest that the decrease rate in the plug length is inversely related to the initial precursor film thickness (which is initially set equal to the trailing film thickness h_1) for this range of Laplace number, pressure drop, and precursor film thicknesses.

Figure 8(a) shows the pressure distribution and wall shear stress along the wall for $h_2 = 0.05$ and $h_2 = 0.09$. The snapshots are taken at times when the plug length, L_p, becomes 0.3 as was done by Fujioka *et al.* [8]. Substantial variations in both wall pressure and wall shear stresses are observed around $0.6 \leqslant x \leqslant 1.0$, which is around the minimum thickness at the front meniscus region. The minimum peak for pressure ($P_w = -3.3$) occurs at $x = 0.66$ for $h_2 = 0.09$, whereas its absolute value is slightly increased ($P_w = -3.5$) at $x = 0.72$ for $h_2 = 0.05$. This suggests that the wall pressure increases for smaller initial precursor film thicknesses.

In Figure 8(a), the wall shear stresses have both negative and positive peaks around the front meniscus region, $0.5 \leqslant x \leqslant 0.8$, as a result of a direction change in velocity field in this region. The positive peak for $h_2 = 0.05$, at $\tau_w = 0.52$ is higher than the positive peak for $h_2 = 0.09$, at $\tau_w = 0.38$. The negative peak for both precursor film thicknesses is the same at $\tau_w = -0.57$. Figure 8(a) shows the present solutions with those reported in Reference [8], showing good agreement between the two studies.

3.2. Rupture dynamics

Snapshots of flow fields highlighting pressure contours at various instants of time are presented in Figure 9, for precursor thickness h_2 of 0.06, the rupture occurs at $t = 321$ when plug length, L_P reaches the critical length of 0.1. After the plug ruptures, the newly formed neck between air fingers takes its expected course when it moves away from the centerline.

The maximum magnitude of wall pressure and shear stress occur at the region of minimum film thickness after rupture. This is shown in Figure 10 for $h_2 = 0.06$, where wall shear stress shows two peaks in opposite directions resulting from the movement of the ruptured liquid–gas interface. The wall pressure exhibits a minimum near where the minimum wall shear stress is located. To offer more details, Figures 10 and 11 show the velocity vectors along with pressure contours around the location of the peaks before and after rupture, respectively. It can be observed that the mentioned extreme conditions occur at the right finger of the plug where the thickness is at minimum. Liquid flow through the narrow portion of the film creates a highly localized region of pressure drop, which shows as a global minimum. As the interface is pulled toward the low-pressure region, its curvature there becomes large to accommodate the larger pressure drop across the phase boundary. A recirculation zone is observed following the interface corner due

DOI: 10.1002/fld

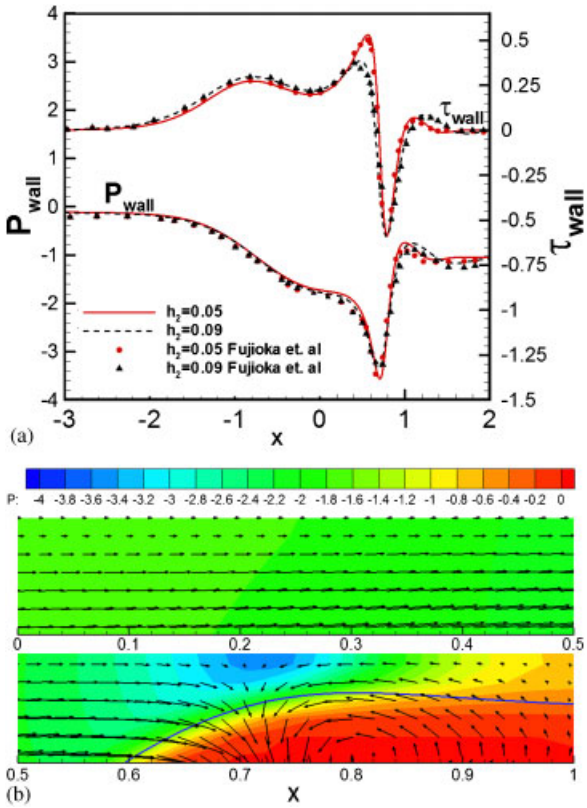

Figure 8. (a) Pressure and shear stress variation at the airway walls before plug rupture when L_p = 0.3, $\Delta P = 1$, and $\lambda = 1000$. Solid lines represent present study while dots represent study of [36]. (b) Pressure contours and velocity vectors near the wall corresponding to $x = 0$–1.

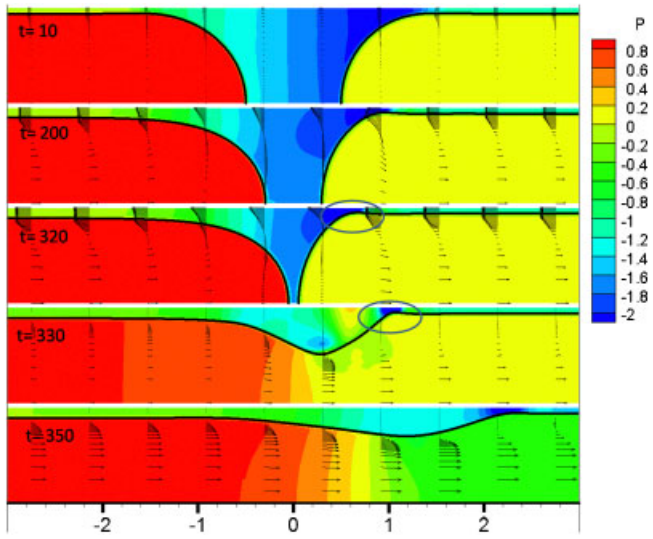

Figure 9. Snapshots of pressure contours before and after rupture. $h_2 = 0.06$, $\Delta P = 1$, and $\lambda = 1000$.

to the surface tension force interaction with the pressure force. The flow reversal explains the opposite directions in wall shear stress.

Once the plug is ruptured, there is a sudden increase in the amount of fluid pushed through the narrow area at the minimum film thickness (to conserve the mass lost by rupture). Fluid accelerates

DOI: 10.1002/fld

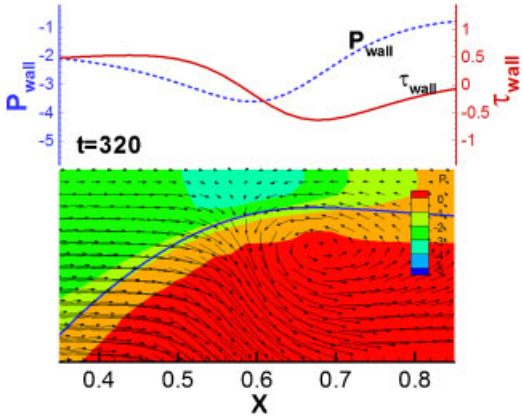

Figure 10. Pressure contours, velocity vectors and wall pressure and wall shear stress prior to rupture for $h_2 = 0.06$. View is zoomed at the location of minimum film thickness.

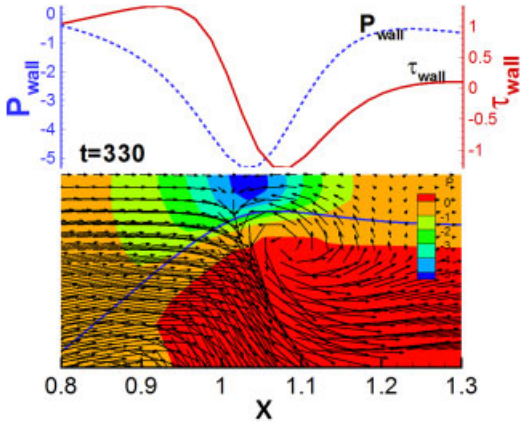

Figure 11. Pressure contours, velocity vectors and wall pressure and wall shear stress after rupture for $h_2 = 0.06$. View is zoomed at the location of minimum film thickness.

causing a larger pressure drop in this area which, in return, pulls the interface and increases its curvature and surface tension force. The dual increase in pressure and surface tension forces causes larger mechanical stresses. This is shown in Figures 9 and 10 where there is an increase in mechanical stresses, velocity, pressure drop, and interface curvature at $t = 330$ (after rupture) compared with $t = 320$ (before rupture). The same behavior during the rupture occurs in other cases at different times. For case with $h_2 = 0.05$, rupture is initiated at $t = 286$. Rupture happens at $t = 376$ when h_2 is 0.07, whereas it is delayed to $t = 482$ with $h_2 = 0.08$ in. Figure 12 shows pressure contour snapshots before and after rupture for $h_2 = 0.08$ and $h_2 = 0.05$.

After the reopening of the tube, the pressure distribution along the streamwise direction changes, eventually becoming linear (namely, approaching a fully developed flow profile) once the effects of rupture diminish. Correspondingly, the liquid flow slows down quickly leading to a sharp change in the wall shear stresses. This is illustrated in Figure 13 for h_2 of 0.06 (other film thicknesses show similar behaviors and are omitted). The dash line shows the wall stresses before rupture. Furthermore, the next recorded time step for pressure and shear stress at the airway walls illustrate that the pressure and shear stress build up at the location where the liquid plug was located. The wall pressure and shear stress show a large variation when compared with their values before the rupture. The x-coordinate in Figure 13 is stationary with its origin fixed at the plug center at the instant of rupture.

The variations of maximum and minimum wall shear stresses in time are presented in Figure 14. The figure shows sudden build-up of wall shear stresses right after the liquid plug rupture, followed

DOI: 10.1002/fld

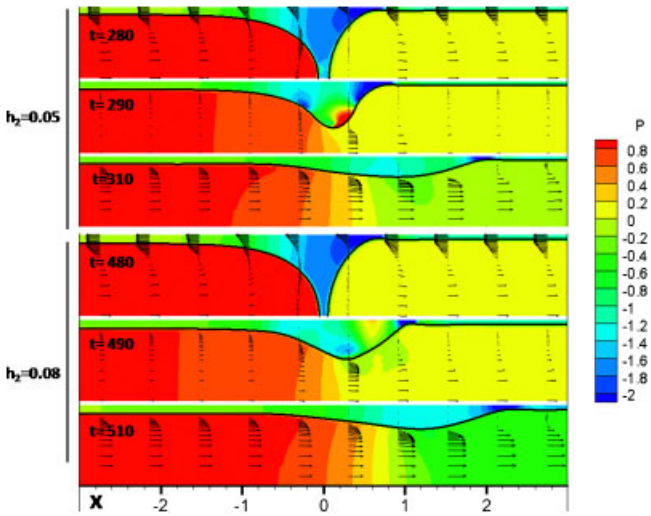

Figure 12. Snapshots of pressure contours before and after rupture. $h_2 = 0.05$, 0.08, $\Delta P = 1$, and $\lambda = 1000$.

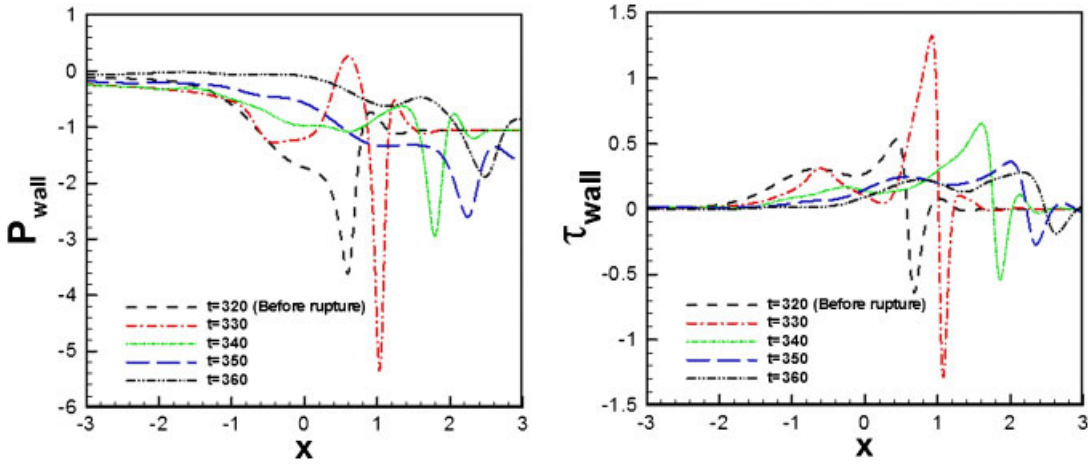

Figure 13. Pressure and shear stresses at the airway walls before and after the rupture. $h_2 = 0.06$, $\Delta P = 1$, and $\lambda = 1000$.

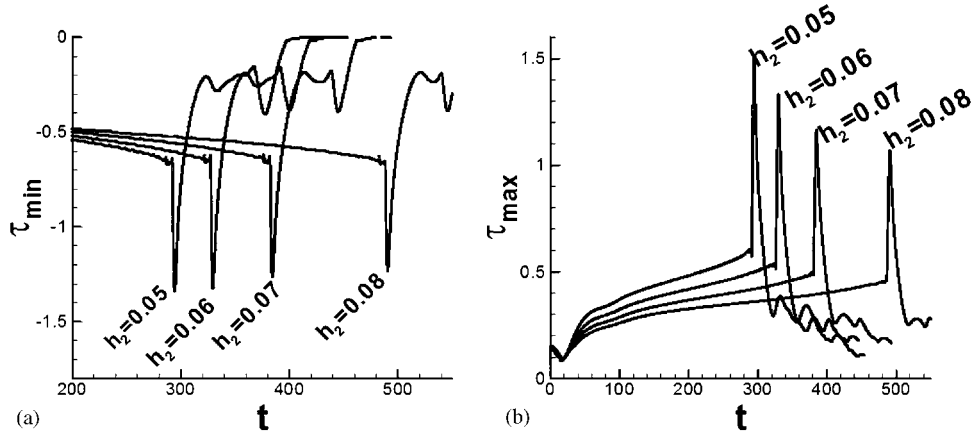

Figure 14. Variation of minimum and maximum wall shear stress in time. $\Delta P = 1$ and $\lambda = 1000$.

DOI: 10.1002/fld

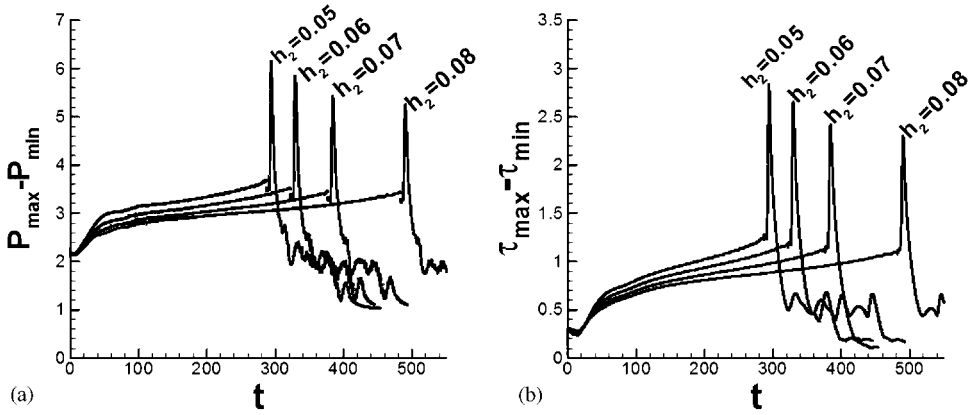

Figure 15. Maximum minimum difference in wall pressure: (a) and wall shear stress, (b) in time. $\Delta P = 1$ and $\lambda = 1000$.

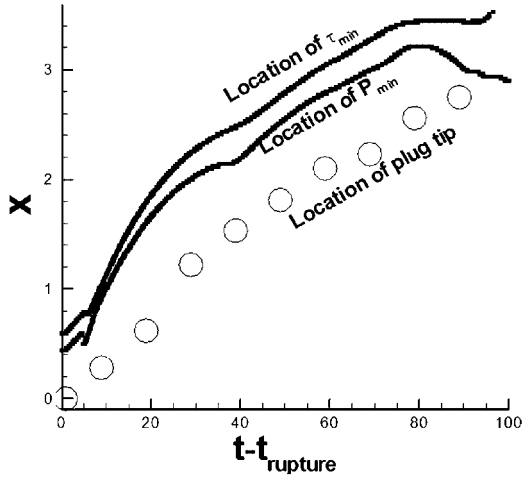

Figure 16. Location of maximum wall shear stress and minimum wall pressure versus ruptured plug. $\Delta P = 1$ and $\lambda = 1000$.

by quick decays. The peak values of wall shear stresses are higher than the values prior to the rupture, and they take finite time to achieve their values after rupture. The variations become larger with smaller initial precursor film thickness values for both pressure and shear stresses at the airway walls. The differences in maximum and minimum values of wall shear stress and pressure are plotted in Figure 15. The maximum difference in wall shear stress is observed for $h_2 = 0.05$ to be 2.7 and decreases slightly for larger h_2 to be 2.3 for $h_2 = 0.08$. Similarly, the maximum difference in wall pressure is observed for $h_2 = 0.05$ to be 6.1 and 4.8 for $h_2 = 0.08$.

It should be noted that the pressure and shear stress in Figure 13 propagate as a wave in the positive x-direction following the plug motion to the right. This is illustrated for h=0.06 case in Figure 16, where the location of the tip of the ruptured plug (defined as the lowest point on the interface) is plotted along with the location of the maximum shear stress. The similarity in the slopes of the two curves indicates that the shear stress wave propagates at about the same speed as the ruptured plug.

Crackles are sounds heard by a stethoscope during a medical examination and categorized into fine and coarse crackles. Fine crackles are characterized by discontinuous, interrupted explosive sounds that are loud and high in pitch [37]. The sound of crackles can be a sign of several diseases including pneumonia, asthma, and interstitial pulmonary fibrosis [37]. There are two possible causes of crackles known by researchers; closures/reopening of airways (i.e. plug rupture) and the collapse of airways due to abnormalities [38].

DOI: 10.1002/fld

The acoustic wave form associated with crackles is shown to have discontinuous sudden peaks [37] similar in behavior to the pressure/shear stress waves in Figure 13 around the time of plug rupture. This suggested link between plug rupture and crackles is in agreement with findings of Munakata *et al.* [39] which shows, experimentally in canine lungs, that the most probable cause for fine crackles is opening and closing of airways rather than abnormal airway collapsibility. Naturally, more rigorous investigation is needed to establish a direct link with quantitative relationships.

3.3. Effects of pressure drop and Laplace number on rupture dynamics

The effects of the initial pressure drop, ΔP, and the Laplace number, $\boldsymbol{\lambda}$, on rupture dynamics are investigated by conducting a parametric study. The pressure drop controls the speed of the plug, and the Laplace number accounts for the fluid properties and tube diameter combinations; they both can influence the rupture and fluid dynamics. Using the case with $h_2 = 0.05$ as a baseline (keeping initial film thickness constant), ΔP is varied keeping all the other non-dimensional parameters constant. Similarly, with ΔP held constant, the Laplace number, λ, is varied to investigate its effect on plug rupture. The cases are summarized in Table I.

Cases 2–6 are studied together with the baseline case to separate the effect of ΔP and cases 7–10 with the baseline are used to study variations in λ. Focusing on the magnitude of wall mechanical stresses, the maximum variations in wall pressure, $P_{\max} - P_{\min}$, and shear stress, $\tau_{\max} - \tau_{\min}$, are used to characterize the effects of the parameters. The time at which rupture occurs is also studied because of its direct relationship with rupture frequency in lung airways.

Figures 17–19 are related to parametric change of initial pressure drop, while Figures 20–22 are related to change in the Laplace number. Figures 17 and 20 show variation of $P_{\max} - P_{\min}$, and shear stress, $\tau_{\max} - \tau_{\min}$ in time. The rupture time is subtracted from the time axis to show when the peaks occur in reference to rupture. In Figure 17(a), the maximum peaks in $P_{\max} - P_{\min}$

Table I. Summary of cases run for parametric study.

Case	ΔP	λ
Baseline	1	1000
2	1/5	1000
3	1/2	1000
4	2/3	1000
5	2	1000
6	3	1000
7	1	200
8	1	500
9	1	2000
10	1	5000

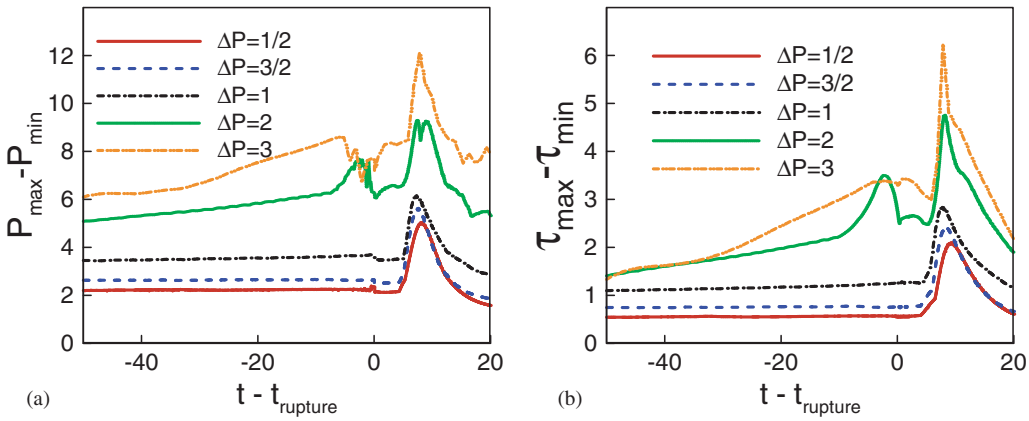

Figure 17. Maximum variations in wall pressure: (a) and shear stress, (b) varying initial pressure drop. $\lambda = 1000$ and $h_2 = 0.05$.

DOI: 10.1002/fld

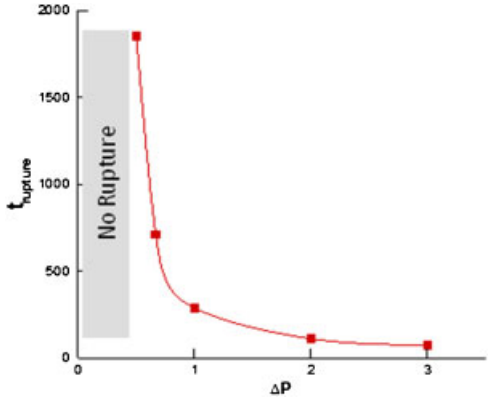

Figure 18. Rupture time versus initial pressure drop (data connected using spline). $\lambda = 1000$ and $h_2 = 0.05$.

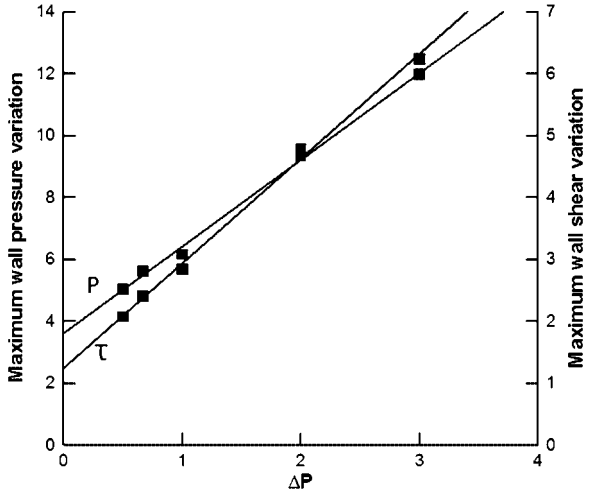

Figure 19. Maximum wall pressure and shear stress variations versus initial pressure drop. $\lambda = 1000$ and $h_2 = 0.05$.

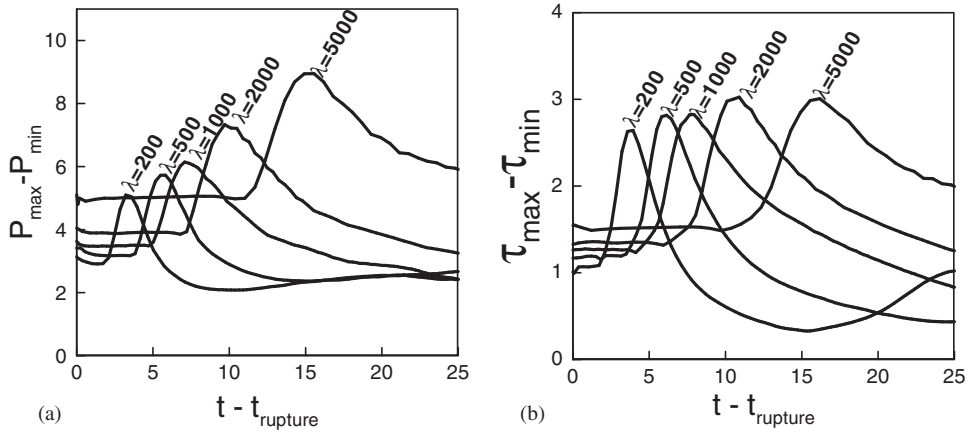

Figure 20. Maximum variations in wall pressure: (a) and shear stress, (b) varying Laplace number. $\Delta P = 1$ and $h_2 = 0.05$.

DOI: 10.1002/fld

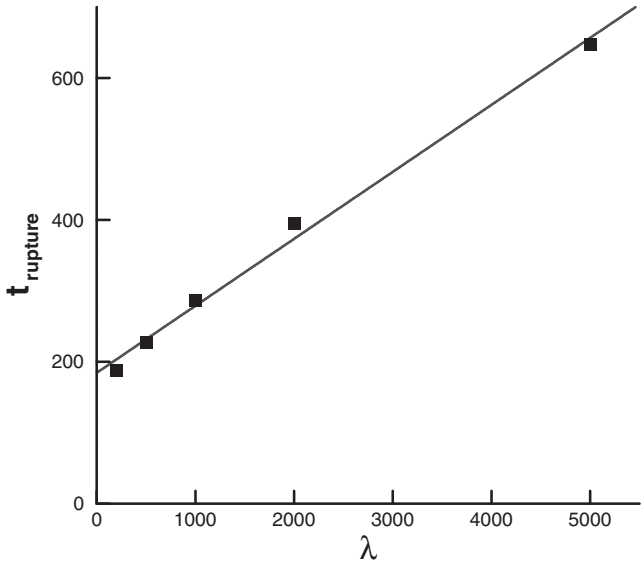

Figure 21. Rupture time versus Laplace number. $\Delta P = 1$ and $h_2 = 0.05$.

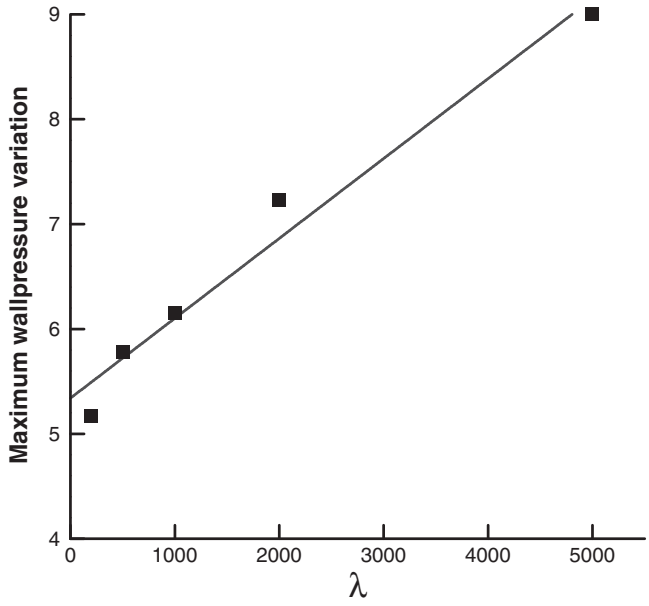

Figure 22. Maximum wall pressure variations versus Laplace number. $\Delta P = 1$ and $h_2 = 0.05$.

increase in magnitude as ΔP increases. Figure 17(b) also shows a similar behavior for $\tau_{max} - \tau_{min}$, with the wall shear stress gradually increasing before rupture in the cases of $\Delta P = 2, 3$. Figure 19 shows the peaks in $P_{max} - P_{min}$, and, $\tau_{max} - \tau_{min}$ versus ΔP. A curve fit shows that the relationship is largely linear, and consequently linearly increases in mechanical stresses in response to pressure build up. The rupture time is plotted versus ΔP in Figure 18, there is a rapid delay in rupture with small pressure drop with a region of no rupture at very small pressure drops (verified by case 2 in which rupture never initiates). As ΔP is increased rupture occurs sooner but appears to reach a plateau of minimum rupture time for very large ΔP.

The maximum variations in wall pressure and shear stress are plotted with respect to rupture time in Figure 20 for Cases 7–10. There is a largely linear increase in the peaks for pressure, as verified in Figure 22; however, the magnitude of the wall shear stress is mainly unaffected. The

DOI: 10.1002/fld

reason for the increase of the wall pressure is that increasing the Laplace number, $\lambda = \rho_l^* \sigma^* R^* / \mu_l^{*2}$ is achieved by increasing the liquid density, which directly affects the wall pressure. There are no significant changes to the flow field (not shown) or the plug shape when λ is varied. Figure 21 shows a linear increase in rupture time when increasing λ. This is because as the Laplace number increases inertia of the liquid increases with respect to the viscosity and it takes longer for the liquid plug to become thinner and to respond to pressure drop.

4. SUMMARY AND CONCLUSION

The present study aims to investigate the dynamics of liquid plug rupture using a novel numerical approach that utilizes a Cartesian grid-based incompressible Navier–Stokes solver with grid adaptation capability. The interface tracking is marker based using the continuous interface method for all constituents to easily allow for large deformations. A new surface reconstruction algorithm triggered by the critical length is developed to allow for plug rupture. The algorithm developed is verified against another numerical study on liquid plug propagation by Fujioka *et al.* [36]. The benchmark study employs a single-fluid formulation on a Lagrangian framework and is limited to simulation prior to rupture. The presented numerical approach ameliorates this limitation and investigates the dynamics of the liquid rupture for various initial precursor film thickness values. The results have shown the following:

- There is an overall agreement when compared with the study of Fujioka *et al.* [36] prior to rupture. The plug length and plug velocity are in reasonable agreement, while the wall pressure and shear stress are a very good match. Discrepancies between the two studies are probably due to different boundary condition implementations and different numerical approaches.
- The liquid plug rupture causes a sudden build up in the mechanical stresses at the airway walls, which can cause damage to the tissues. The magnitude of these stresses reaches its peak at a finite time after the rupture occurs. After reaching the peak values they decrease in magnitude and follow the ruptured plug as it vanishes. The sudden peaks in mechanical stresses suggest a link between plug rupture and crackles that should be further investigated by comparing the acoustics.
- The post-rupture flow field shows a low-pressure region near the wall at the right finger of the plug. This low-pressure region exhibits a global minimum and increases the interface curvature as it is pulled toward it. After rupture, assuming steady flow of air, a fully developed behavior is observed.

Parametric variation shows that the peak values increase when the initial precursor film thickness decreases with a constant Laplace number of 1000 and a unity non-dimensional pressure drop. With a constant initial film thickness and Laplace number, there is a linear relationship between the initial pressure drop and maximum wall mechanical stresses. For high initial pressure drop, there is an increase in wall shear prior to rupture due to small thickness, h_2, region created by the interface shape. Higher initial pressure also resulted in earlier plug rupture. With the pressure drop and the initial film thickness held constant, increasing the Laplace number causes a delay in rupture due to an increase in inertial effects.

REFERENCES

1. Huh D *et al.* Acoustically detectable cellular-level lung injury induced by fluid mechanical stresses in microfluidic airway systems. *Proceedings of the National Academy of Sciences* 2007; **104**:18886.
2. Uzgoren E *et al.* Computational modeling for multiphase flows with spacecraft application. *Progress in Aerospace Sciences* 2007; **43**:138–192.
3. Shyy W *et al. Computational Fluid Dynamics with Moving Boundaries*. Dover, Taylor & Francis: New York, Washington, DC (1996, revised printing 1997, 1998 & 2001), 2007.
4. Tryggvason G, Prosperetti A. *Computational Methods for Multiphase Flow*. Cambridge University Press: Cambridge, 2007.
5. Osher S, Fedkiw RP. *Level Set Methods and Dynamic Implicit Surfaces*. Springer: Berlin, 2002.

DOI: 10.1002/fld

6. Tryggvason G *et al.* A front-tracking method for the computations of multiphase flow. *Journal of Computational Physics* 2001; **169**:708–759.
7. Scardovelli R, Zaleski S. Direct numerical simulation of free-surface and interfacial flow. *Annual Review of Fluid Mechanics* 1999; **31**:567–603.
8. Fujioka H, Takayama S, Grotberg JB. Unsteady propagation of a liquid plug in liquid lined tube. *Physics of Fluids* 2008; **20**:062104.
9. Wasekar VM, Manglik RM. Short-time-transient surfactant dynamics and Marangoni convection around boiling nuclei. *Journal of Heat Transfer* 2003; **125**:858–866.
10. Perot B, Nallapati R. A moving unstructured staggered mesh method for the simulation of incompressible free-surface flows. *Journal of Computational Physics* 2003; **184**:192–214.
11. Sussman M *et al.* A sharp interface method for incompressible two-phase flows. *Journal of Computational Physics* 2007; **221**:469–505.
12. Losasso F, Fedkiw R, Osher S. Spatially adaptive techniques for level set methods and incompressible flow. *Computers and Fluids* 2006; **35**:995–1010.
13. Francois M, Shyy W. Micro-scale drop dynamics for heat transfer enhancement. *Progress in Aerospace Sciences* 2002; **38**:275–304.
14. Uzgoren E, Sim J, Shyy W. Marker-based, 3-D adaptive cartesian grid method for multiphase flow around irregular geometries. *Communications in Computational Physics* 2009; **5**:1–41.
15. Singh R, Shyy W. Three-dimensional adaptive Cartesian grid method with conservative interface restructuring and reconstruction. *Journal of Computational Physics* 2007; **224**:150–167.
16. Shyy W. Multiphase computations using sharp and continuous interface techniques for micro-gravity applications. *Comptes Rendus Mecanique* 2004; **332**:375–386.
17. Peskin CS. The immersed boundary method. *Acta Numerica* 2003; **11**:479–517.
18. Francois M, Shyy W. Computations of drop dynamics with the immersed boundary method, part 1: numerical algoritm and buoyancy-induced effect. *Numerical Heat Transfer. Part B*: *Fundamentals* 2003; **44**:101–118.
19. Ye T *et al.* An accurate Cartesian grid method for viscous incompressible flows with complex immersed boundaries. *Journal of Computational Physics* 1999; **156**:209–240.
20. Leveque RJ, Li Z. The immersed interface method for elliptic equations with discontinuous coefficients and singular sources. *SIAM Journal on Numerical Analysis* 1994; **31**:1019–1044.
21. Li Z, Lai MC. The immersed interface method for the Navier–Stokes equations with singular forces. *Journal of Computational Physics* 2001; **171**:822–842.
22. Ye T, Shyy W, Chung JC. A fixed-grid, sharp-interface method for bubble dynamics and phase change. *Journal of Computational Physics* 2001; **174**:781–815.
23. Uzgoren E, Sim J, Shyy W. Computations of multiphase fluid flows using marker-based adaptive, multilevel Cartesian grid Method. *The 45th AIAA Aerospace Sciences Meeting and Exhibit*, Reno, NV, 2007.
24. Bilek AM, Dee KC, Gaver DP. Mechanisms of surface-tension-induced epithelial cell damage in a model of pulmonary airway opening. *Journal of Applied Physiology* 2003; **94**:770–783.
25. Kay SS *et al.* Pressure gradient, not exposure duration, determines the extent of epithelial cell damage in a model of pulmonary airway reopening. *Journal of Applied Physiology* 2004; **97**:269–276.
26. Zheng Y, *et al.* Liquid plug propagation in flexible microchannels: a small airway model. *Physics of Fluids* 2009; **21**:071903.
27. Howell PD, Waters SL, Grotberg JB. The propagation of a liquid bolus along a liquid-lined flexible tube. *Journal of Fluid Mechanics* 2000; **406**:309–335.
28. Waters SL, Grotberg JB. The propagation of a liquid bolus along a liquid-lined flexible tube. *Physics of Fluids* 2002; **14**:471–480.
29. Fujioka H, Grotberg JB. Steady propagation of a liquid plug in a two-dimensional channel. *Journal of Biomechanical Engineering* 2004; **126**:567.
30. Fujioka H, Grotberg J. The steady propagation of a surfactant-laden liquid plug in a two-dimensional channel. *Physics of Fluids* 2005; **17**:082102.
31. Suresh VA, Grotberg JB. The effect of gravity on liquid plug propagation in a two-dimensional channel. *Physics of Fluids* 2005; **17**:031507.
32. Zheng Y *et al.* Effects of inertia and gravity on liquid plug splitting at a bifurcation. *Journal of Biomechanical Engineering* 2006; **128**:707.
33. Campana DM *et al.* Accurate representation of surface tension using level-contour reconstruction method. *Journal of Computational Physics* 2007; **203**:493–516.
34. Erneux T, Davis SH. Nonlinear rupture of free films. *Physics of Fluids A*: *Fluid Dynamics* 1993; **5**:1117.
35. Uzgoren E *et al.* A unified adaptive cartesian grid method for solid-multiphase fluid dynamics with moving boundaries. *The 18th AIAA Computational Fluid Dynamics Conference*, Miami, FL, 2007.
36. Fujioka H, Takayama S, Grotberg JB. Unsteady propagation of a liquid plug in liquid lined tube. *Physics of Fluids* 2008; **20**. DOI: 10.1063/1061.2938381.
37. Raymond M. In defense of the stethoscope. *Respiratory Care* 2008; **53**:355–369.
38. Pasterkamp H, Kraman SS, Wodicka GR. Respiratory sounds. advances beyond the stethoscope. *American Journal of Respiratory and Critical Care Medicine* 1997; **156**:974–987.
39. Munakata M *et al.* Production mechanism of crackles in excised normal canine lungs. *Journal of Applied Physiology* 1986; **0161**:1120–1125.

DOI: 10.1002/fld